physica status solidi pss rrl
www.pss-rapid.com

Phase-Change Heterostructures Based on Antimony

*Simone Ritarossi, Riccardo Piombo, Flavio Giuliani, Daniele Dragoni, Marco Bernasconi, and Riccardo Mazzarello**

Phase-change materials (PCMs) are employed in optical and electronic storage devices and are interesting candidates for neuromorphic computing. However, they exhibit some drawbacks that limit their application in this field, including a temporal drift in resistance and a stochastic variability of the conductance. To eliminate these problems, it has been proposed to use phase-change heterostructures made of alternating thin layers of PCMs and proper confinement materials, such as transition metal dichalcogenides. Herein, superlattice heterostructures consisting of $TiTe_2$ and antimony are investigated by ab initio methods and neural-network interatomic potentials. The structural and kinetic properties of the relevant phases are characterized. A complete switching cycle is simulated and it is shown that very high quenching rates must be used to generate stable amorphous Sb layers. It is also shown that it is possible to switch the Sb layer without destroying the crystalline structure of $TiTe_2$, which makes these superlattices potential candidates for neuro-inspired applications that do not require long retention times, such as computing-in-memory tasks.

1. Introduction

Phase-change materials (PCMs)[1,2] are employed in nonvolatile memories and are potential candidates for neuromorphic computing devices.[2,3] Upon application of proper electrical pulses, PCMs undergo rapid transitions between a crystalline and an amorphous state, as well as a number of partly crystalline, partly amorphous intermediate states with different resistivity values. These properties enable the implementation of in-memory computing tasks[4] and the emulation of integrate-and-fire[5] and synaptic behavior.[6] Nevertheless, PCM-based memory cells suffer from the resistance drift of the amorphous state due to structural relaxation and from intercell and intracell conductance variability.[7] Several approaches have been pursued to mitigate these problems.[8,9] One of them is based on phase-change heterostructures (PCHs), which consist of alternately grown nanolayers of a PCM and a confinement material.[10–14] In ref. [10], it was shown that $TiTe_2/Sb_2Te_3$ heterostructures exhibit promising properties, including reduced cell variability and drift. Recent density functional theory (DFT) simulations of $TiTe_2$/GeTe and $TiTe_2/Ge_2Sb_2Te_5$ superlattices indicate that, on the time scales accessible by ab initio methods, these two PCMs can also be switched by a controlled heating and quenching protocol, without destroying the crystalline CM layer.[14]

In this work, we consider a superlattice made of alternating nanolayers of antimony and trilayers of $TiTe_2$. Bulk Sb is not a good PCM, since it crystallizes very rapidly even at ambient conditions. However, the stability of its amorphous state can be dramatically enhanced upon nanoconfinement.[15–19] Furthermore, being a pure element, its use should eliminate problems related to unwanted deviations from the optimal stoichiometry, which affect more chemically complex PCMs in ultrascaled devices. Thus, in principle, $TiTe_2$/Sb heterostructures may combine the beneficial effects of nanoconfinement and compositional simplicity of the PCM. We simulate a complete SET–RESET cycle by ab initio molecular dynamics (AIMD). We also investigate the structural and kinetic properties of the crystalline state and of the partial liquid and amorphous states (consisting of liquid/amorphous Sb and crystalline $TiTe_2$). Furthermore, following an approach already employed for GeTe-based superlattices,[20] we mimic the $TiTe_2$/Sb superlattice by means of a machine-learned potential for Sb to study large-scale models and assess finite-size effects in the DFT simulations.

2. Results and Discussion

We consider a superlattice heterostructure made of active PCM nanolayers of pure Sb interspersed with trilayers of the transition-metal dichalcogenide $TiTe_2$, serving as CM. First, we construct a fully crystalline PCH model. Antimony and $TiTe_2$ have different in-plane lattice parameters. To accommodate the lattice mismatch, we create a large supercell by 1) replicating the PCM and CM equilibrium unit cells 6×6 and 7×7

S. Ritarossi, R. Piombo, F. Giuliani, R. Mazzarello
Department of Physics
Sapienza University of Rome
00185 Rome, Italy
E-mail: riccardo.mazzarello@uniroma1.it

D. Dragoni,[+] M. Bernasconi
Department of Materials Science
University of Milano-Bicocca
20125 Milan, Italy

The ORCID identification number(s) for the author(s) of this article can be found under https://doi.org/10.1002/pssr.202500012.

[+]Present address: Leonardo S. p. A., 00195 Rome, Italy

DOI: 10.1002/pssr.202500012

times, respectively, and 2) applying a small in-plane strain to the antimony slab to match the two subsystems. In the resulting model, the in-plane lattice parameters of the PCM slab deviate from the equilibrium values by only 0.2%. The system comprises 435 atoms, with 288 Sb atoms forming four bilayers along the [111] direction and 147 atoms forming the $TiTe_2$ barrier. Additionally, we introduce "vacuum layers" between the two compounds with an initial thickness of 3.5 Å, which we refer to as van der Waals (vdW) gaps. These gaps separate the CM and PCM blocks periodically along the vertical direction.

We optimize the internal structure of the PCH at zero temperature using the QUICKSTEP code within the CP2K package[21] alongside scalar-relativistic Goedecker–Teter–Hutter pseudopotentials.[22] We use the Perdew–Burke–Ernzerhof functional[23] complemented with Grimme-D3 (DFT-D3) vdW corrections[24] to describe the weak chemical interactions within the vdW gaps. The resulting relaxed heterostructure, as depicted in **Figure 1**, has lattice parameters of $a = b = 26.316$ Å, $c = 22.653$ Å, $\alpha = \beta = 90°$, and $\gamma = 120°$, where a, b, and c denote the modules of the three lattice vectors of the supercell, while α, β, and γ represent the supercell angles.

The optimization of the lattice parameters leads to the emergence of distinctive features near the vdW gaps, which are in between those observed in the two PCHs studied in ref. [14]: the $Ge_2Sb_2Te_5/TiTe_2$ PCH exhibits nearly perfect gaps with interfacial interaction equal to 108 meV per atom, whereas the $GeTe/TiTe_2$ PCH displays significant atomic plane corrugation within the vdW gaps and stronger interaction (182 meV per atom). The $Sb/TiTe_2$ PCH shows small atomic corrugation at the vdW gaps, yet with chemical interactions (174 meV atom^{-1}) akin to the GeTe case.

To investigate the stability of our PCH at higher temperatures, we perform AIMD simulations within the canonical ensemble utilizing both Born–Oppenheimer MD and the second-generation Car-Parrinello MD method developed by Kühne et al.[25] We employ the same protocol as in ref. [14]. The initial increase in temperature brings the system to $T = 600$ K, which is less than the melting points of the bulk Sb (904 K) and the bulk $TiTe_2$ (1470 K). At this temperature, the two compounds still maintain their crystalline features, as evidenced by the total radial distribution function (RDF) $g(r)$ shown in **Figure 2**.

To calculate the thickness of the vdW gap, we determine the average position of the PCM and CM interfaces by identifying the local maxima of the histogram of the atomic density profile $\rho(z)$. The vdW gap is then defined as the spatial region between the nearest maxima of the $\rho(z)$ of the PCM and CM. We use a Gaussian filter to improve the accuracy of the peak values. Despite the system remains crystalline, the vdW gaps shrink due to thermal disorder and remain spatially symmetric on average, as noted in **Table 1**.

We now focus on the initial phase of the RESET process, which is a crucial part of the thermodynamic cycle undergone by the PCM in a hypothetical Sb-based PCH device. It involves melting the crystalline Sb layers through a sufficiently strong electrical pulse. Our analysis also allows us to assess the stability of the superlattice structure at temperatures that surpass the melting point of Sb. We progressively increase the temperature from 600 to 1700 K and run a 10 ps simulation at this elevated temperature to induce rapid melting. Notably, the crystalline structure of the CM remains stable throughout this brief simulation, despite the temperature exceeding its melting point. Subsequently, we lower the temperature to 1300 K, resulting in the complete melting of the PCM in ≈50 ps. In Figure 2a, we present a snapshot illustrating the liquid structure of confined Sb alongside the crystalline structure of the CM. The latter can also be verified by inspecting the CM's RDF at $T = 1300$ K in Figure 2b. Regarding the vdW gap thickness at 1300 K, we find that $L_{GAP}^{(1)} = 3.06$ Å and $L_{GAP}^{(2)} = 3.17$ Å.

We analyze the structural properties of confined liquid Sb (l-Sb) by comparing them with those derived from a bulk model of pure Sb. The initial crystalline structure of the bulk model consists of periodic repetitions along the c direction of the crystalline Sb slab of our PCH model. We subject the bulk system to the same thermodynamic cycle undergone by the PCH. In Figure 2c, we compare the RDFs $g_{Sb}(r)$ of bulk and confined l-Sb. As expected for liquid phases, the two RDFs show a large peak at short distances, followed by a steady decay to the constant value of 1 at longer distances. Both $g_{Sb}(r)$ are truncated at ≈5.5 Å, which is the appropriate correlation length for our bulk system. We determine the first maxima $\bar{r}$ and minima r_{cut} of the RDFs, which represent the most probable atomic bond lengths and the size of the first coordination shell, respectively. Given that the RDFs do not display a minimum but rather a shoulder, we set $r_{cut} = 3.5$ Å, for both confined and bulk systems. The main features of the two RDFs turn out to be very similar, including the positions of their maxima: for confined l-Sb we obtain $\bar{r} = 3.038$ Å while in bulk l-Sb $\bar{r} = 3.062$ Å. These values are

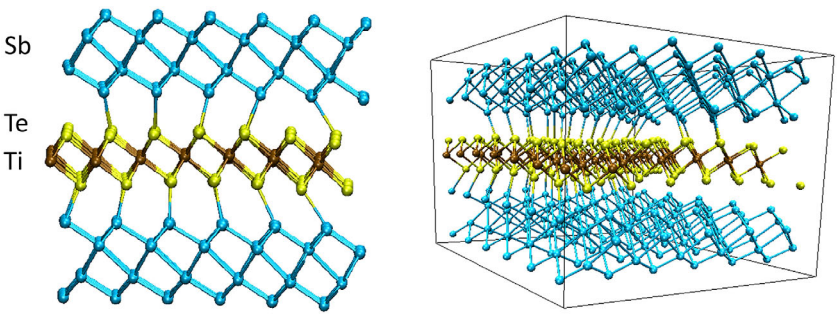

Figure 1. The relaxed model of Sb/TiT_2 at $T = 0$ K. Te, Ti, and Sb atoms are depicted in yellow, brown, and cyan respectively. One can observe small corrugations at the interfaces between antimony and TiT_2.

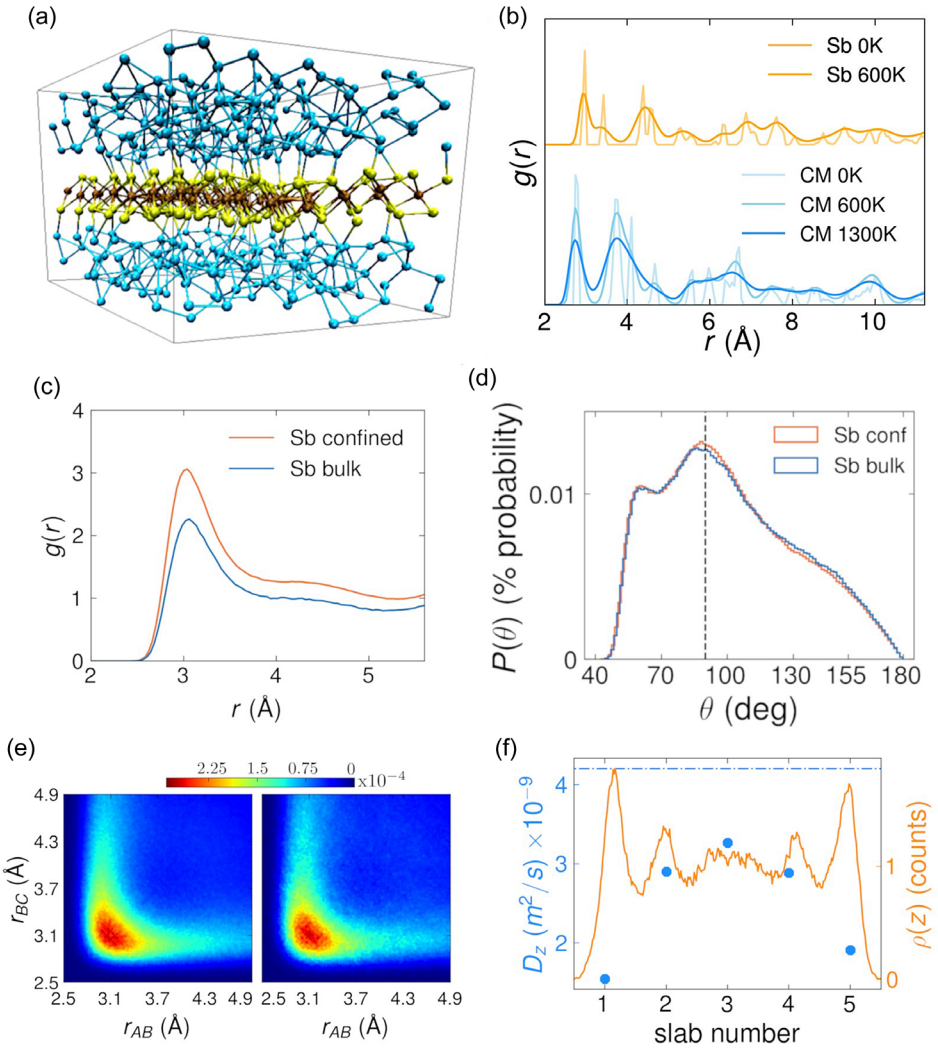

Figure 2. a) The partially liquid model of $Sb/TiTe_2$ at $T = 1300$ K. One can observe that the crystalline structure of the CM is preserved. b) The RDFs of the confined Sb and $TiTe_2$ at $T = 0$, 600, and 1300 K; the zero-temperature RDFs have their amplitude halved to facilitate comparison with the ones at higher temperatures. The higher the temperature, the broader the peaks become due to the increased thermal motion of the atoms. c,d) The RDFs and ADFs of liquid Sb at $T = 1300$ K in the confined (orange curves) and bulk (blue curves) case; the black dashed line in the right plot is centered at 90°. e) The ALTBC plots of liquid Sb at $T = 1300$ K in the confined (left plot) and bulk (right plot) case. f) Profile of the D_z self-diffusion coefficient of the *l*-Sb atoms inside the PCH at $T = 1300$ K. The PCM region is divided into slabs and the D_z values are given for each slab (blue points). The dash–dotted line refers to the $D_z^{(bulk)}$ value of 4.30×10^{-9} m s^{-2}. We also report the atomic density profiles $\rho(z)$ of the *l*-Sb atoms at $T = 1300$ K along the *z* direction (orange curve).

Table 1. Thicknesses $L_{GAP}^{(1)}$ and $L_{GAP}^{(2)}$ of the first and second vdW gap of the $Sb/TiTe_2$ PCH at $T = 0$ K, 600 K, and 300 K. All the thicknesses are expressed in Å. The meaning of prot. 1 and prot. 2 is clarified in the discussion of the quenching protocols in the main text.

	0 K (crystalline)	600 K (crystalline)	300 K (amorphous-prot. 1)	300 K (amorphous-prot. 2)
$L_{GAP}^{(1)}$	3.08	3.14	3.29	3.08
$L_{GAP}^{(2)}$	3.04	3.04	3.20	3.12

slightly higher than the average nearest-neighbor separation in confined crystalline Sb at 0 K, as indicated by the first peak at 2.92–2.97 Å in Figure 2b.

The simulations for the liquid phase reproduce the main features of the experiments of ref. [26] very well, including the position of the maximum (which they estimated to be around 3.05 Å) and the existence of a barely visible hump at around 4.15 Å. Indeed, the hump's height vanishes as temperature raises, as reported in ref. [26]. If we take 4.15–4.2 Å as a reasonable radial position of the maximum of the hump, the ratio of that quantity to the position of the first peak is ≈1.36–1.38 in both cases. This has been interpreted as indicating a distortion of a simple-cubic-like structure in *l*-Sb.[27] Indeed, in a simple cubic-like system the ratio of the next-nearest-neighbor distance to the nearest-neighbor one is approximately equal to $\sqrt{2} \approx 1.414$.

We emphasize that the absolute values of the RDFs for the two liquid systems in Figure 2c cannot be directly compared due to

the different supercell volumes involved. However, it is meaningful to compare the total coordination numbers (CNs) N_{Sb}. By integrating the RDFs up to r_{cut}, we obtain $N_{Sb} = 4.69$ and 5.39 for confined and bulk *l*-Sb, respectively. In ref. [28], $N_{Sb} = 5.05$ at $T = 1300$ K was reported for bulk *l*-Sb; however, a different r_{cut} (3.2 Å) was used.

In Figure 2d we show the angular distribution function (ADF) of confined and bulk *l*-Sb, where the same cutoff $r_{cut} = 3.5$ Å is employed. The ADF indicates that the local structure of the liquid phase for both systems is characterized by octahedral (bond angles around 90° and nearly linear configurations) and triangular configurations (bond angles around 55°–60°).

We also examine the tail end of the ADF ranging from 155° to 180°. Specifically, we analyze nearly aligned atomic triplets through the angular-limited three-body correlation (ALTBC) function $g_3(r_{AB}, r_{BC})$ defined as

$$g_3(r_{AB}, r_{BC}) = \frac{1}{\mathcal{N}} \sum_{i,j,k} \left\langle \delta(r_{AB} - r_{ij}) \delta(r_{BC} - r_{ik}) \theta(\beta + \gamma) \right\rangle \quad (1)$$

where θ represents the Heaviside function, $\gamma \in (0, 25°)$, $\beta = \pi - \alpha$, with α being the bond angle, $\mathcal{N} = (4\pi)^2 r_{AB}^2 r_{BC}^2$ is a normalization factor, and the brackets denote an average over all configurations from the AIMD simulations. In the Figure 2e, we display the ALTBCs of confined and bulk *l*-Sb. All ALTBC plots show a single broad peak centered on the diagonal ($r_{AB} = r_{BC}$), indicating that the majority of atomic triplets do not exhibit Peierls-like distortions.

Next, we study the kinetic properties of the PCM. We determine the self-diffusion coefficient D_z along the vertical direction (referred to as the *z*-direction) of the *l*-Sb atoms at $T = 1300$ K employing Einstein's formula.

$$D_z = \frac{1}{2} \lim_{t \to \infty} \frac{d}{dt} \left\langle \mathrm{MSD}_z(t) \right\rangle \quad (2)$$

where MSD_z represents the mean square displacements of the *l*-Sb atoms along the *z* direction. Here, the notation $\langle \cdot \rangle$ indicates an average over the trajectory of each atom throughout the AIMD simulation. To obtain a reliable value for D_z, we fit the averaged $\mathrm{MSD}_z(t)$ using a linear function in the range where it exhibits a linear profile with respect to time. Specifically, the function $\mathrm{MSD}_z(t)$ is defined as

$$\mathrm{MSD}_z(t) = \frac{1}{T_{run} - t} \sum_{i=0}^{T_{run}-t} [z(i+t) - z(i)]^2 \quad (3)$$

where T_{run} denotes the length of the entire AIMD simulation, *z* represents the vertical position of an *l*-Sb atom, and *i* and *t* are time lag indices. In Equation (2), the ensemble average is evaluated by averaging all contributions to the MSD in Equation (3) that pertain to the same time lag.

Equation (3) is a tool to analyze the global D_z value of *l*-Sb atoms, both in confined and bulk scenarios. Our analysis reveals that the confinement of Sb atoms results in a reduced D_z value. Specifically, we observe $D_z^{(conf)} = 2.21 \times 10^{-9} \mathrm{m^2\,s^{-1}}$ in the confined case and $D_z^{(bulk)} = 4.30 \times 10^{-9} \mathrm{m^2\,s^{-1}}$ in the bulk scenario.

To delve deeper into the influence of confinement and interface effects on diffusion, we compute the D_z value for confined *l*-Sb atoms for varying distances from the vdW gaps. We use the same approach as in ref. [14]. We exclude the region occupied by the CM, which maintains its crystalline characteristics, as depicted in Figure 2a, and has a negligible self-diffusion coefficient. Subsequently, we partition the region occupied by *l*-Sb into multiple slabs parallel to the *xy* plane. The segmentation is guided by the atomic density profiles $\rho(z)$ illustrated in Figure 2f: a slab corresponds to the volume between two density minima. We establish a total of five slabs with varying thicknesses, as evidenced in Figure 2f: the central slab and the two outermost ones are 4 Å wide, while the remaining slabs are 3 Å wide.

Confinement results in larger D_z values for the *l*-Sb atoms in the central slab, located farther from the CM, while at the interface with the CM, D_z decreases toward 0, as illustrated in Figure 2f. Even at the center of the slabs, the D_z profile remains lower than the corresponding bulk value (represented by dash–dotted lines in Figure 2f) due to finite-size effects. Throughout the MD simulations at 1300 K, which span more than ≈50 ps, no *l*-Sb atom penetrates the CM trilayer. Although the *l*-Sb atoms diffuse near the boundaries, they all rebound; the CM acts as a barrier against the migration of *l*-PCM atoms along the *z* direction. This phenomenon also influences the shape of $\rho(z)$, with the *l*-Sb atoms clustering at the edges of the PCM blocks. These findings align with the simulations of $Sb_2Te_3/TiTe_2$ PCHs presented by Ding et al. in ref. [10] and with our own simulations of $Ge_2Sb_2Te_5/TiTe_2$ PCHs and $GeTe/TiTe_2$ PCHs.[14]

The amorphous phase is achieved by rapidly quenching the system from the previously obtained partially liquid state. Prior studies on bulk Sb models have shown that the quenching rate used to generate the amorphous phase significantly influences the system's ability to recrystallize and the crystallization speed.[15] In our simulations, we employ two distinct protocols: in the first protocol (prot. 1), the system is quenched at a rate of 10^{15} K s^{-1} from 1300 to 900 K and then further cooled at rate 10^{13} K s^{-1} from 900 to 300 K. We employed this protocol in our previous work.[14] In the second protocol (prot. 2), a single rate of 10^{15} K s^{-1} is applied from 1300 to 300 K. The rationale behind using a single, ultrahigh rate is that prot. 1 results in partially crystallized Sb at the interfaces (**Figure 3**); this incipient crystallization begins to emerge around 600 K, during the second cooling stage. By adopting prot. 2, we are able to produce a fully amorphous confined Sb.

In Figure 3 the models produced with the two protocols are compared, showing that prot. 1 (left model) leads to a Sb slab with partial crystalline order at the interfaces. The RDFs for the two models shown in Figure 3 do not differ much. They both display a first peak at 2.97 Å, while the second peak is at 4.33 and 4.28 Å for prot. 1 and 2, respectively. The CNs N_{Sb} for the Sb atoms are equal to $N_{Sb} = 4.09$ with $r_{cut} = 3.50$ Å for prot. 1 and $N_{Sb} = 4.31$ with $r_{cut} = 3.5$ Å for prot. 2. Examining the ADF in the inset of Figure 3 one observes that, for prot. 1, there is a notable excess of bonds at ≈90° compared to the fully amorphous PCM (prot. 2).

We further characterize the model generated using prot. 1, focusing on the crystalline nucleus in the shaded region in Figure 3. We compare this region with the metastable cubic phase of bulk antimony. This phase was simulated using

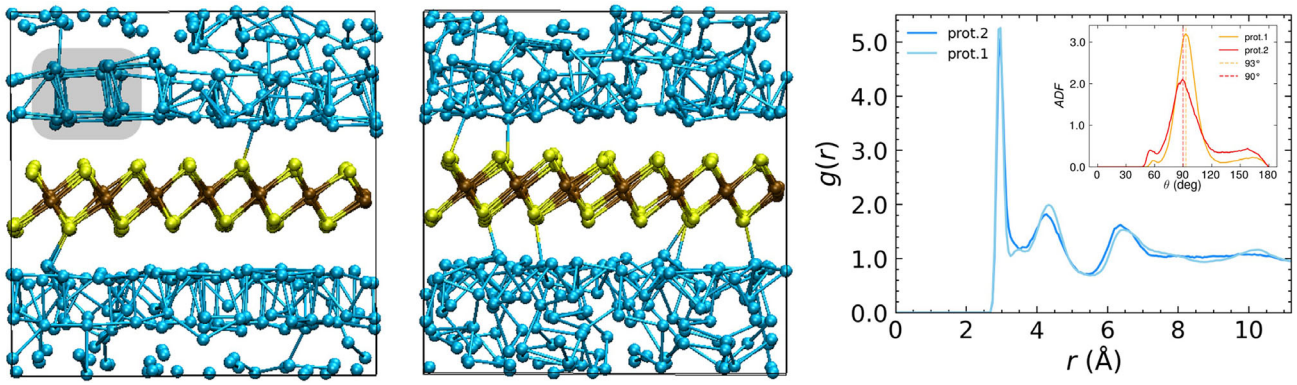

Figure 3. (left) The quenched model of the PCH at 300 K, generated using DFT and prot. 1 (double quenching rate). The confined PCM clearly displays layering and, notably, partial crystallization at the interfaces: the shaded region highlights the crystalline part. (middle) The PCH model with fully amorphous PCM at 300 K, produced using prot. 2 (single quenching rate). No crystalline region is observed in the Sb slab. (right) The RDFs for the PCM regions of the two models obtained with prot. 1 and prot. 2 do not show significant differences, whereas the ADFs (inset) show a larger number of bonds at ≈90° for prot. 1.

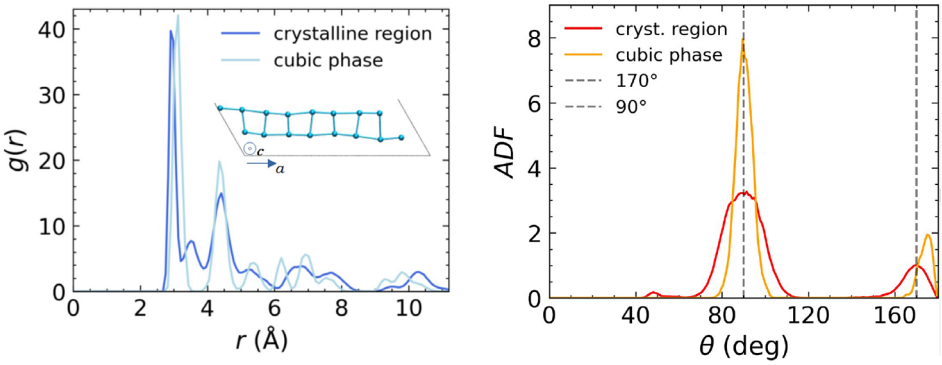

Figure 4. (left) The RDFs at 300 K of the crystalline region of the Sb slab extracted from the PCH model (dark blue) and of the cubic bulk phase of antimony (light blue); the comparison reveals a distorted structure in the confined model. The inset depicts a snapshot of the crystalline region of the slab, which forms a chain parallel to the *a*-axis. (right) The ADFs at 300 K for the crystalline region display broader peaks at 90° and at 170° than the ones of the cubic bulk phase, confirming the presence of pronounced distortions in this region.

CP2K at 300 K after performing a structural relaxation of the system. The results are shown in **Figure 4**. The relaxed structure exhibits a lattice parameter of 3.11 Å. This value aligns with the position of the RDF peak associated with the first coordination shell, as shown in Figure 4. Subsequent RDF maxima are observed at $3.11\sqrt{2}$ and $3.11\sqrt{3}$ Å, respectively. The ADF, calculated with a cutoff of $r_{cut} = 3.2$ Å (shown in Figure 4, right), reveals a pronounced peak at 90° alongside an additional contribution near 180°. This reflects a perfectly cubic symmetry with only minimal distortions.

When compared to the crystalline region of the PCM at 300 K, notable differences emerge. The crystalline region in the PCH reveals a highly distorted pseudocubic structure, with distance of $\bar{r}_1 = 2.91$ Å for the first shell and $\bar{r}_2 = 3.51$ Å for the second shell. In the ADF, while the main peak at 90° persists (calculated with an extended $r_{cut} = 3.9$ Å to include the second RDF shell), it appears broader. The second, smaller peak is slightly shifted to smaller angles (170°). The inset of Figure 4 provides a snapshot of the crystalline region, viewed along the *a*-axis perpendicular to the plane represented in Figure 3. It highlights an alternation between short and long bonds, specifically four short and four long bonds along the *a*-axis. Therefore the distances $\bar{r}_1$ and $\bar{r}_2$ correspond to these short and long bonds, respectively.

Following the previous structural analysis of the crystalline region and the insights provided by the snapshot in Figure 3, we argue that the recrystallized PCM adopts a pseudocubic configuration. In this arrangement, the *c* axis of the PCH supercell corresponds to the (100) direction of the (pseudo-)cubic lattice and a fully crystalline layer would consist of 7×8 atoms. Indeed these dimensions are the only combination that matches the lattice parameters of the supercell.

To generate long trajectories of a few ns and to assess potential finite-size effects, we have also created two "artificial" models of the $TiTe_2$/Sb superlattice, in which the confinement layers are replaced by frozen trilayers of Sb constrained at the lattice parameters of $TiTe_2$. These models contain only Sb atoms and thus enable the use of a relatively simple neural network (NN) potential for the description of the Sb–Sb interactions. In recent years, machine-learned potentials have proven to be a very valuable tool to investigate the switching kinetics of PCMs.[29–35] Here we use the NN potential for Sb presented in ref. [16], which allows a speed-up of the simulations by several orders of magnitude

compared to AIMD. In our MD simulations, the thickness of the gaps between the PCM and the frozen CM in the initial fully crystalline model was set to 3.1 Å. A similar approach was recently employed to investigate $TiTe_2$/GeTe superlattices.[20]

The first model matches the DFT model in both atom count and lattice parameters. The second model contains 2604 atoms, 2016 of which form the PCM slab. Specifically, model 2 was obtained by doubling the a and b lattice parameters of model 1 and by adding six additional Sb layers along the c direction. This results in a heterostructure with lattice parameters of $a = b = 52.63$ Å, $c = 33.98$ Å, and a PCM thickness of ≈23 Å. For both NN-based models, we employed the same melting–quenching protocol used for the DFT model. After thermalizing the NN models at 600 K for 100 ps, we melted the PCM by heating it to 1300 K and thermalizing for 100 ps. Subsequently, we exclusively applied protocol 2 (single-rate) for quenching, cooling the systems to 300 K and thermalizing them for 100 ps. In the upper part of **Figure 5**, snapshots of model 1 and 2 at 300 K are shown.

No crystalline regions are observed in the PCM slab of both models, in agreement with the results obtained for the DFT model with prot. 2 (single rate). Furthermore, the amorphous regions have similar structural properties as those in the said DFT model.

We now explore the crystallization dynamics of these models in detail. We ran a 200 ps trajectory at 600 K for the quenched DFT model with a crystalline Sb region (prot. 2). On this time scale, this region extends until it form an almost complete crystalline bilayer at the interface; nevertheless, the remaining part of the Sb slab does not crystallize. Thus, in the following, we discuss the models based on the NN potentials, which enable longer simulations. The two models are reheated to two distinct target temperatures, 500 and 600 K. For model 1, the simulations are run for 10 ns at both temperatures. This model does not show any recrystallization at 500 K. On the contrary, at 600 K it initially forms a 7×8 pseudocubic bilayer at one of the interfaces (within ≈500 ps), similarly to the DFT model, and latter forms a second 7×8 crystalline bilayer within 2.5 ns, as shown in Figure 5, bottom. The two bilayers are staggered along the ab plane. This structure persists for the remaining 7.5 ns of the trajectory. We note that the PCM slab contains 288 atoms and each crystalline bilayer comprises 112 atoms. The remaining 64 atoms form a disordered layer at the second interface. The first bilayer interacts weakly with the second, which in turn intermittently exchanges atoms with the disordered layer, resulting in very low atomic diffusion even after 2.5 ns, with coefficients given by $D_z^{(PCM)} = 1.1 \times 10^{-12}\,\mathrm{m\,s^{-2}}$, $D_{x,y}^{(PCM)} = 7.8 \times 10^{-11}\,\mathrm{m\,s^{-2}}$. These diffusion coefficients, calculated over the last 7.5 ns of the trajectory at 600 K, are 2–3 orders of magnitude lower than those obtained for the liquid phase of the PCM.

In model 2, the system (see **Figure 6**) achieves crystallization even at 500 K, in contrast to model 1, showing that finite-size effects play an important role in the latter model. Within 600 ps, the structure forms four pseudocubic bilayers with an additional disordered layer. The bilayers are staggered with respect to each other, forming three stacking faults. Since each atomic layer consists of $14 \times 16 = 224$ atoms, in principle the PCM slab could fully crystallize (unlike model 1) and form nine crystalline layers. Indeed, after 750 ps, the disordered layer also crystallizes, albeit rotated relative to the other layers. This behavior might stem from the instability of trilayer Sb structures. The resulting structure remains stable throughout the subsequent 9.25 ns of the trajectory.

At 600 K, the recrystallization process starts with the formation of three pseudocubic bilayers within 500 ps, leaving the remaining three layers disordered. By 1.2 ns, these layers also

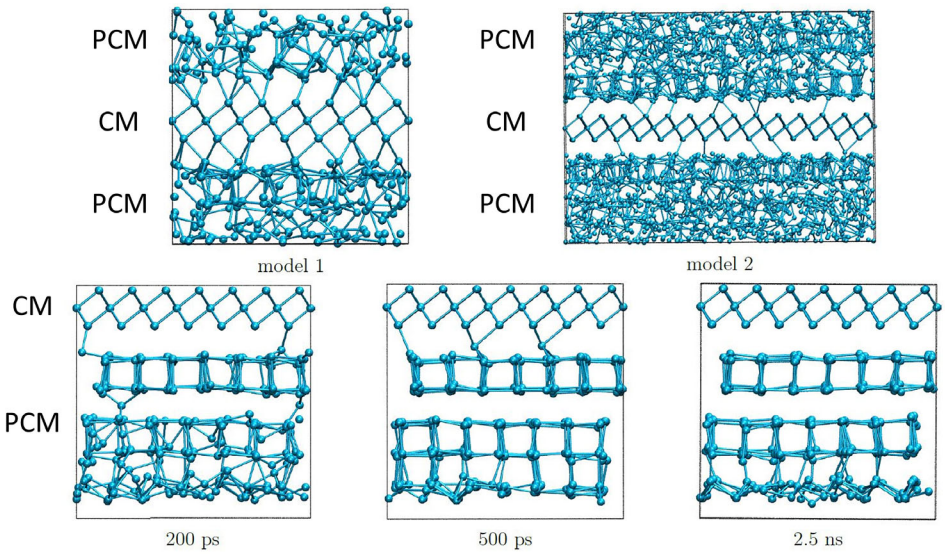

Figure 5. (top) NN-based model 1 (left snapshot) and model 2 (right snapshot) at 300 K, obtained using protocol 2 (single-rate). The snapshots indicate that no crystalline regions form in the PCM slab, consistent with the behavior seen in the DFT model. This is confirmed by an analysis of the local structure based on bond-order parameters (not shown). (bottom) Three snapshots of the trajectory for model 1 at 600 K. For better visualization of the crystallization process, the cell has been selected so that the CM trilayer appears in the upper part. The snapshots show the emergence of a structure consisting of two staggered pseudocubic bilayers and an additional disordered monolayer near the lower interface.

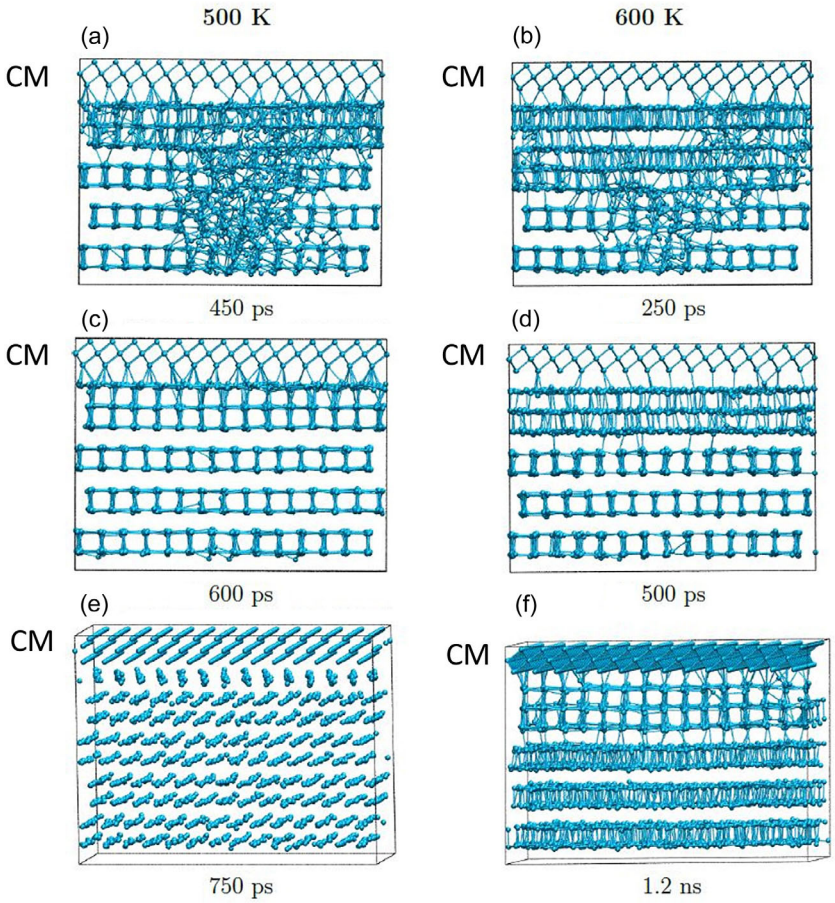

Figure 6. The trajectories of model 2 at a) 500 K (left) and b) 600 K (right) show that a large portion of the system has recrystallized after c) 600 ps and d) 500 ps, respectively. e,f) At longer times, the monolayer at the upper interface also becomes ordered, although it is rotated with respect to the bottom layers.

recrystallize, once again exhibiting a rotational stacking fault. This phase remains stable throughout the subsequent 8.8 ns. We have also analyzed the structural properties (**Figure 7**) of two crystalline regions extracted from the two NN models: the resulting RDFs and ADFs show an almost perfect match with those of the crystalline region from the DFT model under prot. 1. This makes us confident that the crystalline structure obtained upon recrystallization is not an artifact of the NN simulations but a genuine metastable phase. Using the NN potential, we have also computed the energy difference between our recrystallized models and 1) the initial, fully crystalline PCHs consisting of alternating layers of the artificial CM and the stable crystalline phase of Sb and 2) the PCHs obtained upon fast quenching to room temperature, which consist of alternating

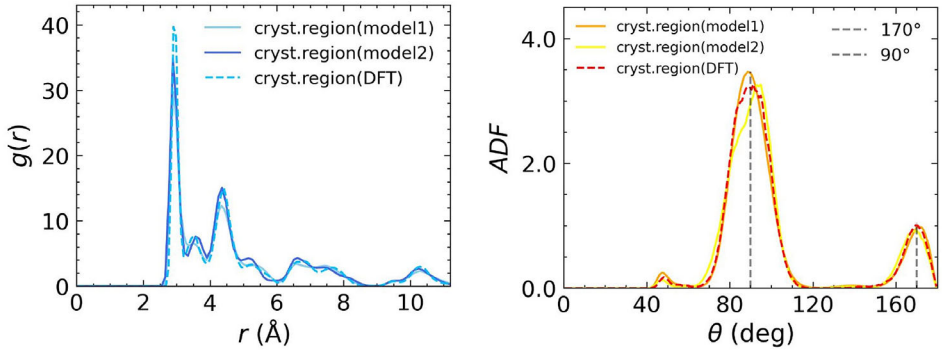

Figure 7. $g(r)$ and ADF of two crystalline regions extracted from model 1 and model 2 at 600 K, compared to those of the DFT model. The comparison reveals an almost perfect match, underscoring the pseudocubic geometry of the recrystallized phase.

layers of the artificial crystalline CM and amorphous Sb. It turns out that the energy of the recrystallized models is only 2–4 meV per atom (depending on the model) higher than the one of the PCH with the stable crystalline Sb. Furthermore, the recrystallized models are significantly more stable than the partly amorphous PCHs (energy difference: 32–49 meV per atom depending on the model). These findings suggest that the formation of the layered phase is stabilized by the interaction with the CM.

3. Conclusion

In conclusion, we have investigated models of $Sb/TiTe_2$ superlattices containing nanolayers of antimony and trilayers of $TiTe_2$. We have shown that, upon relaxation, the fully crystalline model exhibits small atomic corrugation and moderate chemical interaction (174 meV $atom^{-1}$) at the vdW gaps. Subsequently, we have simulated a complete switching cycle, consisting of 1) melting and amorphization of the Sb layer (so called RESET process) without melting of the $TiTe_2$ trilayer and 2) recrystallization of the Sb layer (SET process). Our simulations indicate that it is possible to switch the Sb layer without destroying the confinement layer. Nevertheless, very high quenching rates must be employed to avoid partial recrystallization of the active layer during the RESET process. These findings suggest that nanoconfinement by $TiTe_2$ does not increase the stability of amorphous Sb significantly, which may hinder the experimental realization of a partly amorphous $Sb/TiTe_2$ heterostructure. We also note that the timescales accessible by our simulations are short (nanoseconds). Furthermore, our initial models correspond to ideal, defect-free superlattices. In real device setups, the switching pulses may destroy the confinement layers.[36] Therefore, both the growth conditions and the heating protocols must be controlled very carefully to avoid these issues.

Acknowledgements

The authors gratefully acknowledge funding from the PRIN 2020 project "Neuromorphic devices based on chalcogenide heterostructures" funded by the Italian Ministry for University and Research (MUR). This work was supported by the ICSC—Centro Nazionale di Ricerca in High Performance Computing, Big Data, and Quantum Computing funded by European Union—NextGenerationEU. The authors acknowledge the CINECA award under the ISCRA and ICSC initiatives for the availability of high-performance computing resources and support. The authors thank Y. Chen for useful discussions.

Open access publishing facilitated by Universita degli Studi di Roma La Sapienza, as part of the Wiley - CRUI-CARE agreement.

Conflict of Interest

The authors declare no conflict of interest.

Author Contributions

Simone Ritarossi: data curation (lead); formal analysis (lead); investigation (lead); methodology (lead); software (supporting); validation (lead); visualization (lead); writing—original draft (equal). **Riccardo Piombo**: formal analysis (equal); methodology (equal); software (equal); validation (equal); visualization (supporting); writing—original draft (equal). **Flavio Giuliani**: formal analysis (supporting); methodology (supporting); validation (supporting). **Daniele Dragoni**: methodology (equal); software (equal). **Marco Bernasconi**: formal analysis (supporting); methodology (equal); software (equal); supervision (supporting). **Riccardo Mazzarello**: conceptualization (lead); formal analysis (equal); investigation (equal); methodology (equal); resources (lead); supervision (lead); writing—original draft (lead).

Data Availability Statement

The data that support the findings of this study are available from the corresponding author upon reasonable request.

Keywords

monoatomic phase-change memories, neuromorphic computing, phase-change heterostructures

Received: January 10, 2025
Revised: February 6, 2025
Published online: February 24, 2025

[1] S. Raoux, W. Welnic, D. Ielmini, *Chem. Rev.* **2010**, *110*, 240.
[2] W. Zhang, R. Mazzarello, M. Wuttig, E. Ma, *Nat. Rev. Mater.* **2019**, *4*, 150.
[3] D. Marković, A. Mizrahi, D. Querlioz, J. Grollier, *Nat. Rev. Phys.* **2020**, *2*, 499.
[4] A. Sebastian, M. Le Gallo, R. Khaddam-Aljameh, E. Eleftheriou, *Nat. Nanotechnol.* **2020**, *15*, 529.
[5] T. Tuma, A. Pantazi, M. Le Gallo, A. Sebastian, E. Eleftheriou, *Nat. Nanotechnol.* **2016**, *11*, 693.
[6] D. Kuzum, R. G. Jeyasingh, B. Lee, H.-S. P. Wong, *Nano Lett.* **2012**, *12*, 2179.
[7] L. Crespi, A. Lacaita, M. Boniardi, E. Varesi, A. Ghetti, A. Redaelli, G. D'Arrigo, in *2015 IEEE International Memory Workshop (IMW)*, Monterey, CA, USA **2015**, pp. 1–4.
[8] W. W. Koelmans, A. Sebastian, V. P. Jonnalagadda, D. Krebs, L. Dellmann, E. Eleftheriou, *Nat. Commun.* **2015**, *6*, 8181.
[9] S. Ambrogio, P. Narayanan, H. Tsai, R. M. Shelby, I. Boybat, C. Di Nolfo, S. Sidler, M. Giordano, M. Bodini, N. C. Farinha, B. Killeen, C. Cheng, Y. Jaoudi, G. W. Burr, *Nature* **2018**, *558*, 60.
[10] K. Ding, J. Wang, Y. Zhou, H. Tian, L. Lu, R. Mazzarello, C. Jia, W. Zhang, F. Rao, E. Ma, *Science* **2019**, *366*, 210.
[11] X. Wang, Y. Wu, Y. Zhou, V. L. Deringer, W. Zhang, *Mater. Sci. Semicond. Process.* **2021**, *135*, 106080.
[12] X. Wang, K. Ding, M. Shi, J. Li, B. Chen, M. Xia, J. Liu, Y. Wang, J. Li, E. Ma, Z. Zhang, H. Tian, F. Rao, *Mater. Today* **2022**, *54*, 52.
[13] X. Wu, A. I. Khan, H. Lee, C.-F. Hsu, H. Zhang, H. Yu, N. Roy, A. V. Davydov, I. Takeuchi, X. Bao, H.-S. P. Wong, E. Pop, *Nat. Commun.* **2024**, *15*, 1.
[14] R. Piombo, S. Ritarossi, R. Mazzarello, *Adv. Sci.* **2024**, *11*, 29.
[15] M. Salinga, B. Kersting, I. Ronneberger, V. P. Jonnalagadda, X. T. Vu, M. Le Gallo, I. Giannopoulos, O. Cojocaru-Mirédin, R. Mazzarello, A. Sebastian, *Nat. Mater.* **2018**, *17*, 681.
[16] D. Dragoni, J. Behler, M. Bernasconi, *Nanoscale* **2021**, *13*, 16146.
[17] S. Aggarwal, T. Milne, N. Farmakidis, J. Feldmann, X. Li, Y. Shu, Z. Cheng, M. Salinga, W. H. Pernice, H. Bhaskaran, *Nano Lett.* **2022**, *22*, 3532.
[18] B. Chen, X. Wang, F. Jiao, L. Ning, J. Huang, J. Xie, S. Zhang, X. Li, F. Rao, *Adv. Sci.* **2023**, *10*, 25.

[19] X. Shen, Y. Zhou, H. Zhang, V. L. Deringer, R. Mazzarello, W. Zhang, *Nanoscale* **2023**, *15*, 15259.
[20] D. Acharya, O. Abou El Kheir, D. Campi, M. Bernasconi, *Sci. Rep.* **2024**, *14*, 1.
[21] T. D. Kühne, M. Iannuzzi, M. Del Ben, V. V. Rybkin, P. Seewald, F. Stein, T. Laino, R. Z. Khaliullin, O. Schütt, F. Schiffmann, D. Golze, J. Wilhelm, S. Chulkov, M. Hossein Bani-Hashemian, V. Weber, U. Borštnik, M. Taillefumier, A. S. Jakobovits, A. Lazzaro, H. Pabst, T. Müller, R. Schade, M. Guidon, S. Andermatt, N. Holmberg, G. K. Schenter, A. Hehn, A. Bussy, F. Belleflamme, G. Tabacchi, et al., *J. Chem. Phys.* **2020**, *152*, 19.
[22] S. Goedecker, M. Teter, J. Hutter, *Phys. Rev. B* **1996**, *54*, 1703.
[23] J. P. Perdew, K. Burke, M. Ernzerhof, *Phys. Rev. Lett.* **1996**, *77*, 3865.
[24] S. Grimme, J. Antony, S. Ehrlich, H. Krieg, *J. Chem. Phys.* **2010**, *132*, 15.
[25] T. D. Kühne, M. Krack, F. R. Mohamed, M. Parrinello, *Phys. Rev. Lett.* **2007**, *98*, 066401.
[26] Y. Greenberg, E. Yahel, E. N. Caspi, B. Beuneu, M. P. Dariel, G. Makov, *J. Chem. Phys.* **2010**, *133*, 9.
[27] A. Chiba, M. Tomomasa, T. Higaki, T. Hayakawa, R. Takahashi, K. Tsuji, *J. Phys. Conf. Ser.* **2008**, *121*, 022019.
[28] R. O. Jones, O. Ahlstedt, J. Akola, M. Ropo, *J. Chem. Phys.* **2017**, *146*, 19.
[29] G. C. Sosso, G. Miceli, S. Caravati, J. Behler, M. Bernasconi, *Phys. Rev. B* **2012**, *85*, 17.
[30] F. C. Mocanu, K. Konstantinou, T. H. Lee, N. Bernstein, V. L. Deringer, G. Csányi, S. R. Elliott, *J. Phys. Chem. B* **2018**, *122*, 8998.
[31] Y. Zhou, W. Zhang, E. Ma, V. L. Deringer, *Nat. Electron.* **2023**, *6*, 746.
[32] Y.-J. Choi, M. Ghim, S.-H. Jhi, *Phys. Rev. Mater.* **2024**, *8*, 1.
[33] O. Abou El Kheir, L. Bonati, M. Parrinello, M. Bernasconi, *npj Comput. Mater.* **2024**, *10*, 1.
[34] Y. Chen, D. Campi, M. Bernasconi, R. Mazzarello, *Adv. Funct. Mater.* **2024**, *34*, 22.
[35] O. R. Dunton, T. Arbaugh, F. W. Starr, *J. Chem. Phys.* **2025**, *162*, 3.
[36] G. M. Cohen, A. Majumdar, C. Cheng, A. Ray, D. Piatek, L. Gignac, C. Lavoie, A. Grun, H. Cheng, Z. Liu, H. Lung, H. Miyazoe, R. L. Bruce, M. BrightSky, *Phys. Status Solidi RRL* **2024**, *18*, 2300426.